



CHALMERS

Chalmers Publication Library

On the Numerical Modeling of Impinging Jets Heat Transfer - A Practical Approach

This document has been downloaded from Chalmers Publication Library (CPL). It is the author's version of a work that was accepted for publication in:

Numerical Heat Transfer, Part A Applications (ISSN: 1040-7782)

Citation for the published paper:

Bovo, M. ; Davidson, L. (2013) "On the Numerical Modeling of Impinging Jets Heat Transfer - A Practical Approach". Numerical Heat Transfer, Part A Applications, vol. 64(4), pp. 290-316.

<http://dx.doi.org/10.1080/10407782.2013.784113>

Downloaded from: <http://publications.lib.chalmers.se/publication/179395>

Notice: Changes introduced as a result of publishing processes such as copy-editing and formatting may not be reflected in this document. For a definitive version of this work, please refer to the published source. Please note that access to the published version might require a subscription.

Chalmers Publication Library (CPL) offers the possibility of retrieving research publications produced at Chalmers University of Technology. It covers all types of publications: articles, dissertations, licentiate theses, masters theses, conference papers, reports etc. Since 2006 it is the official tool for Chalmers official publication statistics. To ensure that Chalmers research results are disseminated as widely as possible, an Open Access Policy has been adopted. The CPL service is administrated and maintained by Chalmers Library.

(article starts on next page)

On the numerical modeling of impinging jets heat transfer. A practical approach

Mirko Bovo^{1,2} and Lars Davidson¹

¹ Dept. of Applied Mechanics, Chalmers University of Technology, 41296 Gothenburg, Sweden

² Powertrain Analysis, Volvo Car Corporation, 40531 Gothenburg, Sweden

Abstract

This paper compares steady-state and transient simulations in predicting impinging jet heat transfer. The configurations tested are $H/D=2$ and 6 , Re 10000, 20000, 23000, 30000. The variables considered are: Turbulence model (LES, $k-\epsilon$, $k-\omega$, V2F), discretization schemes, mesh density and topology, inlet velocity profile and turbulence. The V2F model performs best for the steady state simulations. The inlet velocity profile plays an important role. Mesh topology and distribution is also important. The turbulence created in the shear layer plays a stronger role than the inlet turbulence. The LES model reproduces the turbulent structures with a useful degree of accuracy.

Nomenclature

D diameter (m)

H nozzle-to-wall distance (m)

k turbulent kinetic energy (m^2/s^2)

Nu Nusselt number

r radius (m)

Re Reynolds number

u' , v' , w' : velocity fluctuation (m/s)

W_b bulk inlet velocity (m/s)

y^+ dimensionless wall distance

z height (m)

Greek symbols

μ molecular viscosity (kg/m^2s)

μ_t turbulent viscosity (kg/m^2s)

ϵ turbulence dissipation rate (m^2/s^3)

Acronyms

LES Large Eddy Simulation

rms root mean squared

RANS Reynolds Averaged Navier-Stokes

URANS Unsteady RANS

Introduction

Impinging jets flows have remarkable features and find many applications in industry. Consequently, this type of flow has been an object of interest for many researchers. However, part of the physics governing impinging jet flows is not fully understood and this prevents a satisfying prediction of the effects of an arbitrary jet configuration.

A particularly interesting aspect of impinging jets is the heat transfer occurring between the fluid and the impingement wall. This convective phenomenon gives rise to the highest levels of heat transfer coefficient known for single phase flows. Moreover, the heat transfer changes significantly with respect to the position on the target wall.

Impinging jets have been studied in a number of configurations varying in geometrical and dynamic parameters. The dynamic variables basically are related to the jet velocity and turbulence intensity [3, 5, 6, 9, 11].

Historically, impinging jets have been studied analytically and experimentally. Later, numerical simulations have also been deployed in this field. Numerical simulations are nowadays an established method to study and predict fluid flows. Therefore, they are widely used for product development in industry. In CFD (Computational Fluid Dynamics), new turbulence models are applied to generic, well documented cases to evaluate their performance. Often the models are tested in simplified conditions, for example performing 2D simulations. However, there is a risk that well-performing models in such simplified conditions will fail to work for real industrial applications due to numerical instability or poor robustness. On the other hand, even if a model fails to accurately predict absolute values, it might still be able to correctly predict trends, which is certainly relevant for practical applications. Therefore, robust models such as the $k-\epsilon$ are still widely used in industry and considered in this work.

Impinging jets are notoriously difficult to model in CFD. The flow features of the near wall region are challenging to capture with the near wall assumptions commonly implemented in the models. Moreover, the flow field presents strong curvatures, unsteadiness and strong pressure strain stresses. The combination of these features makes it difficult to accurately predict the impinging jet flow and consequently its associated convective heat transfer. For these reasons impinging jets are recommended as a test case for CFD models [16].

Attempts to study impinging jets have been carried out using CFD simulations with varying degrees of success, some examples are found in [7, 13, 14, 17, 18]. The general conclusion is that the more detailed the model is, the better it can capture the flow feature. However, detailed models are increasingly computationally expensive and are more likely to encounter stability problems.

The first part of this work, addresses impinging jets with a steady state (time averaged) approach. The influence of several variables is systematically studied using a factorial design of experiment approach. The second part extends the study with a transient analysis of stationary impinging jets. The evaluation is not only based on the comparison with experimental data but also on the computational effort necessary to perform the simulation and model stability.

Impinging jet physics

A comprehensive description of impinging jets is presented in [10, 11]. Here a short description is given, in order to bring attention to some important features relevant to the present work. An impinging jet is characterized by a jet flow impacting (impinging) on a surface. The resulting flow field can be divided in three regions (see Figure 1).

- The *free jet region* in which the wall is not affecting the flow field. This region can be further sub-divided in two. 1) The *potential core*, where the flow basically maintains its initial velocity (nozzle outlet velocity). 2) The *shear layer*, where the jet interacts with the surrounding medium exchanging momentum and mass.
- In the *impinging region* the flow strikes the wall and is forced to undergo a sudden change of direction. The *stagnation point* is located at the center of this region.
- The *wall jet region* in which the flow leaving the impinging region develops into a semi-confined flow.

In the jet shear layer large parallel toroidal (donut-like) vortices interact with each other. Under certain flow conditions the vortices merge in an event called “vortex pairing” (see Figure 1), this might be interpreted as a case of turbulence back scattering. Back scattering is the transfer of turbulent kinetic energy from small to larger turbulent structures. This is a known phenomenon that can be found in turbulent flows and it presents a difficulty for common turbulence models, which are designed assuming turbulence to be purely dissipative (i.e. energy flows from large to small turbulent structures).

There are different types and configurations of impinging jets. A distinction can be made by the shape of the nozzle (e.g. circular, slot, square), the upstream flow can be fully or partially developed, and the jet may be confined by an upper wall. In this work *impinging jet* refers to a fully developed turbulent flow discharged from a circular pipe and orthogonally impinging a flat smooth surface. The jet is discharged in a quiescent (still) medium of the same nature as the jet fluid.

The nozzle diameter D is the reference length to characterize jet flows. The most important parameters to describe impinging jets heat transfer are the two dimensionless groups Nusselt Number (Nu) and Reynolds number (Re). Geometrical parameters are nozzle-to-wall spacing (H/D) and radial position (r/D). Another important parameter is inlet turbulence intensity. The final goal of research on impinging jets is to understand the physics governing the phenomenon and correlate all these parameters.

Impinging jet flow has remarkable effects on convective heat transfer. Indeed, this kind of flow has among the highest known levels of Nusselt number (Nu) for single phase flows.

An example of experimental results is proposed in Figure 2. The Nusselt number presents a maximum at the stagnation point. Here the boundary layer thickness is at its minimum, offering the minimum resistance to the heat flux. The Nu then tends to decrease for greater r/D due to the growth of the boundary layer. Moreover, radial flow velocity decreases as the flow spreads to an increasingly larger area.

For relatively high Re and small H/D (e.g. $Re=28000$ and $H/D=2$) the Nusselt number $Nu(r/D)$ presents a secondary peak (Figure 2). This phenomenon is not fully understood despite considerable experimental and numerical efforts [4, 5, 6, 8].

Various explanations are suggested to explain the characteristic secondary peak. One is as follows: the free jet feeds the wall jet region as a column of fluid as shown in Figure 3 (left). In the impingement region the flow diverges in radial direction forcing it to a strong acceleration creating the wall jet region. Strong acceleration holds the boundary layer laminar damping velocity fluctuations normal to the flow. Moreover, in the acceleration zone, the flow is pressed against the wall by the incoming column of fluid. The acceleration results in high velocity which in turn generates high heat transfer likely to be correlated to the secondary peak. As the radial distance increases, the velocity decreases because the cross-sectional area of the flow in the wall jet region increases, and consequently the Nu decreases as well.

An alternative explanation relates to the development of the boundary layer (Figure 3 center). The laminar boundary layer develops from the stagnation point and eventually transitions to turbulent. The transition region is associated with an increase in heat transfer due to the enhancement of mass transfer in the direction normal to the wall. This transition can be associated to the secondary peak in the $Nu(r/D)$.

A third explanation for the secondary peak is that turbulent vortices grow in the shear layer of the free jet. These structures travel in the jet direction and impact on the target surface in a ring around the impingement point (see Figure 3 right). The resulting velocity fluctuations normal to the wall increase the heat transfer affecting the boundary layer structure. This theory is supported by measurements [5, 6] correlating the vortices frequency with the fluctuation of the heat transfer rate.

It is likely that the secondary peak in the Nusselt number curve is attributable to some combination of the three effects presented above. Interestingly, for very small values of H/D a third peak is observed, suggesting that the different phenomena act at different locations [10].

The heat transfer rate depends on the jet inlet conditions such as the velocity profile at the nozzle. Another important parameter is turbulence intensity. High levels of turbulence enhance the momentum diffusion of the jet and consequently reduce the potential core length. The effect of the turbulence is strong enough to eliminate the secondary peak occurring for high Re and small H/D . However, this variable has a lower impact for higher H/D where the turbulence created in the shear layer becomes dominant [10, 11].

Modeling of impinging jets

A CFD model is a complex assembly of a number of interacting sub-models (e.g. turbulence model, numerical discretization). The choice of these sub-parts influences the final result. In this study a number of variables are tested and cross-compared in order to serve as a future reference for setting up an efficient simulation for impinging “jet - like” flows. This section discusses each of the different parts of the model individually.

Space (spatial discretization)

Figure 4 (top) provides an overview of the geometry along with details of the mesh and boundary conditions. The mesh defines how the computational domain is discretized. The geometry is divided in layers in a direction normal to the impingement plane. The size of the cell layer closest to the impingement wall is chosen so that $y^+ < 1$ is satisfied in every location at any time. This condition is necessary to resolve the viscous sub-layer (see zoom-in in Figure 4 top). Further specific details about the mesh are given along with the related results.

The circular shape of the domain is discretized using two different approaches (Figure 4 bottom). The topology called “butterfly” is based on a square outline in the center that is transformed in a circular shape. This topology allows only for refinement in a radial direction for a given partition of the inner square. The “peacock” topology allows for a flexible increase in the number of cells in both the radial and the angular directions. Six meshes are created for the case $H/D=2$ with $0.25E06$, $0.5E06$ and $1E06$ cells for both topologies. The case with $H/D=6$ is solved with three meshes counting $0.125E06$, $0.5E06$ and $2E06$ cells. All these meshes have the same development in the wall-normal direction (see Figure 4).

Further, three meshes are created to study the influence of the cell spacing in the wall-normal direction (Table 1). All meshes have the same size for the first cell near the wall and satisfy the criterion $y^+ < 1$. Moreover all meshes have the same growth rate from the wall. The different meshes vary in the total number of cells and in cell density distribution. Mesh 1 grows through the entire domain with a ratio of 1.06 for a total of $2E6$ cells. Mesh 2 is characterized by a sharp increase in cell high at $H/D=0.5$ with local growth rate of about 2 over one cell layer. The general rule is not to exceed a growth rate of 1.2 but often in practical applications this is overlooked to limit the total cell number. Mesh 2 has the same total number of cells as mesh 1. Mesh 3 grows with ratio 1.06 up to about $H/D=2$. Thereafter it keeps a constant cell size resulting in a total of $2.4E6$ cells.

Time (temporal discretization)

The characteristics of a stationary jet can be meaningfully represented by a time-averaged solution. However, by resolving also the time variation of the flow it is possible to gain a deeper understanding of the phenomena governing the impinging jet. It is also known that some problems related to simulation stability can be overcome by running a transient simulation of a stationary flow. The downside of this approach is that it significantly increases the simulation’s computational cost. An important parameter in transient simulations is the CFL number. Physically, this quantity defines how many cells a fluid particle passes through in a time step. For a robust transient simulation the CFL should be smaller than 1 but, for practical reasons, a larger CFL number is often tolerated. In this

project the time step is chosen so that the CFL number is around 1 for most of the domain, allowing temporary local maxima of about ten.

Inlet, outlet and wall boundary conditions

The outlet boundary condition is *constant pressure* (see Figure 4 top). The upper boundary condition is *slip wall*. *Constant pressure* would be a better boundary condition for the upper wall, but this condition is avoided being more prone to numerical instability. This choice is backed by measurements showing negligible differences in heat transfer between confined and unconfined jets for $H/D \geq 2$ [8]. The boundary condition on the impingement wall is *no slip* with a constant heat flux, reproducing the effect of an electrical resistor as in the experiments.

At the inlet, a velocity profile is prescribed. Both uniform flow (plug flow) and fully developed pipe flow are tested as inlet velocity profile. The velocity profile for fully developed pipe-flow is calculated in a separate simulation and mapped at the inlet boundary. In the finest mesh, the inlet boundary is discretized with 1280 cells. This resolution is fine enough to resolve the largest turbulent structures of the inlet flow. Synthetic turbulent fluctuations are in some cases superimposed to the fully developed turbulent profile.

Inlet synthetic turbulent fluctuations

Turbulent fluctuations are calculated using the method presented in [12]; only a brief overview is provided in this section. The method is specifically designed to generate inlet boundary conditions to LES. The turbulent integral length scale and time scale are derived from the inlet size and the wall shear stress in the pipe. A number of independent synthesized velocity fields are produced by prescribing the turbulent integral length scale. The fields are independent in the sense that their time correlation is zero. When running the simulation, one of the computed velocity fields is superimposed as initial conditions for the inlet. The inlet condition for a given time step N is calculated as a weighted average between the fluctuation field N and the superimposed fluctuation field at $N-1$, the latter being a function of all previously used fields. This interpolation is called an “asymmetric time filter” and is a function of the turbulent integral time scale and the simulation time step.

The result of the application of the method presented above is a space and time correlated field of the velocity fluctuations at the inlet. Figure 5 shows an example of these fluctuations. It can be noticed that the three fluctuation components are of the same order of magnitude. Consequently, at the inlet the cell aspect ratio should be about 1 to properly resolve the fluctuations.

Equations (numerical discretization)

The simulations are carried out using the commercial code Star-CD. This commercial code can be run with its own patented discretization scheme called MARS. This is a 2nd order discretization scheme. The MARS’s ability to capture strong gradients in the flow can be changed by using different settings for the scheme’s compression level. This can be set between 0 and 1. Low values for this parameter result in a more robust model, less prone to diverge or crash. With higher values of this parameter the simulation is able to

more accurately capture sharp gradients in the flow field. The default value for this parameter is 0.5 which is a compromise between accuracy and robustness. The same differentiation scheme is used for all the equations (i.e. momentum, energy and turbulence). The CD (Central Difference) scheme is also tested for comparison.

Turbulence modeling

Impinging jets are a recommended test for the evaluation of turbulence models because they present peculiar turbulent structures [16]. In this work, four different turbulence models are tested as implemented in the commercial code Star-CD 4.08. All models are used in their low-Re form (i.e. no wall function), accordingly the mesh is generated so as to accurately resolve the boundary layer.

k- ε and k- ω model (standard)

A basic assumption is that the effect of turbulence can be accounted for with a scalar isotropic property called turbulent viscosity μ_t (Bousinesq approximation). Turbulent viscosity is calculated locally in the computational domain and is related to the local turbulent length and velocity scales. The production terms in the transport equation of turbulent quantities are related to the local gradients of the mean flow.

The k- ε model results from the implementation of the assumption above. In this model μ_t is derived from the turbulent kinetic energy k and the turbulent dissipation rate ε . Transport equations for these two quantities (k and ε) are solved along with the momentum and the energy equations.

The equation for the turbulent kinetic energy, k , is the same for the k- ε and the k- ω models:

$$\frac{\partial}{\partial t}(\rho k) + \frac{\partial}{\partial x_j} \left[\rho \bar{u}_j k - \left(\mu + \frac{\mu_t}{\sigma_k} \right) \frac{\partial k}{\partial x_j} \right] = \mu_t \left(2S_{ij} \frac{\partial \bar{u}_i}{\partial x_j} \right) - D_k \quad (1)$$

with

$$S_{ij} = \frac{1}{2} \left(\frac{\partial \bar{u}_i}{\partial x_j} + \frac{\partial \bar{u}_j}{\partial x_i} \right) \quad (2)$$

$$\mu_t = f_\mu \frac{C_\mu \rho k^2}{\varepsilon} \quad (3)$$

$$f_\mu = [1 - e^{-0.0198 Re_y}] \left(1 + \frac{5.29}{Re_y} \right) \quad (4)$$

$$Re_y = \frac{y \sqrt{k}}{\nu} \quad (5)$$

$$D_k = \rho \varepsilon \quad (6)$$

where $\varepsilon = \beta^* k \omega$ in the k- ω model. The equations for the turbulent dissipation rate ε for the k- ε model is the following

$$\begin{aligned} \frac{\partial}{\partial t}(\rho\varepsilon) + \frac{\partial}{\partial x_j} \left[\rho u_j \varepsilon - \left(\mu + \frac{\mu_t}{\sigma_\varepsilon} \right) \frac{\partial \varepsilon}{\partial x_j} \right] = \\ C_{\varepsilon 1} \frac{\varepsilon}{k} \left[\mu_t \left(2S_{ij} \frac{\partial u_i}{\partial x_j} + P' \right) \right] + C_{\varepsilon 2} (1 - 0.3e^{-R_t^2}) \rho \frac{\varepsilon^2}{k} + C_{\varepsilon 4} \rho \varepsilon \frac{\partial u_i}{\partial x_i} \end{aligned} \quad (7)$$

with

$$P' = 1.33 [1 - 0.3e^{-R_t^2}] \left[2S_{ij} \frac{\partial u_i}{\partial x_j} + 2 \frac{\mu}{\mu_t} \frac{k}{y^2} \right] e^{-0.00375Re_y^2} \quad (8)$$

A complete description of the k- ε model can be found in [13].

The k- ε model belongs to the family of the two-equations models. A rather extensive study of two-equations models applied to impinging jets is presented in [17]. The general conclusion of the study is that this type of model is not particularly suitable to solve impinging jet flows. In the same work, the specific results for impinging jets with characteristics similar to the present study indicate that the standard k- ε model performs best, giving the heat transfer prediction closest to the experimental data. Moreover, the k- ε model is the most popular among the turbulence models used in industry. For these reasons this model is considered in this investigation.

The equation for the specific dissipation rate ω is

$$\begin{aligned} \frac{\partial}{\partial t}(\rho\omega) + \frac{\partial}{\partial x_j} \left[\rho u_j \omega - \left(\mu + \frac{\mu_t}{\sigma_\omega} \right) \frac{\partial \omega}{\partial x_j} \right] = \\ \alpha \frac{\omega}{k} \mu_t P - \rho \beta \omega^2 + C_{\varepsilon 3} \mu_t P_B C_\mu \omega \end{aligned} \quad (9)$$

$$\begin{aligned} \beta &= \beta_0 f_\beta & \beta^* &= \beta_0^* f_\beta^* & \chi_\omega &= \left| \frac{\Omega_{ij} \Omega_{ik} S_{ki}}{(2\beta_0^* \omega)^3} \right| \\ f_\beta &= \frac{1 + 70\chi_\omega}{1 + 80\chi_\omega} & f_\beta^* &= \begin{cases} 1 & , \chi_k \leq 0 \\ \frac{1 + 680\chi_k^2}{1 + 400\chi_k^2} & , \chi_k > 0 \end{cases} & \chi_k &= \frac{1}{\omega^3} \frac{\partial k}{\partial x_j} \frac{\partial \omega}{\partial x_j} \end{aligned} \quad (10)$$

Turbulent viscosity is given

$$\mu_t = \rho \frac{k}{\omega} \quad (11)$$

A complete description of the k- ε model can be found in [22].

V2F model

The pressure strain affects the turbulent structures in the near wall region of an impinging jet. The V2F model differs from the k- ε model in that it solves for two extra quantities, the wall-normal Reynolds stress v^2 , and f_{22} , which is an equation for the redistribution of v^2 . The V2F model automatically detects the presence of a wall and accounts for its effect on the turbulence.

The k equation in the V2F model is as for the standard k- ε model, the ε equation is

$$\frac{\partial}{\partial x_j} \left[\rho \bar{u}_j \varepsilon - \left(\mu + \frac{\mu_t}{\sigma_\varepsilon} \right) \frac{\partial \varepsilon}{\partial x_j} \right] = \frac{C_{\varepsilon_1}^z}{T_s} \left[\mu_t \left(2S_{ij} \frac{\partial \bar{u}_i}{\partial x_j} \right) \right] - \frac{C_{\varepsilon_2}}{T_s} \rho \varepsilon \quad (12)$$

The v^2 equation is

$$\frac{\partial}{\partial x_j} \left[\rho \bar{u}_j v^2 - \left(\mu + \frac{\mu_t}{\sigma_k} \right) \frac{\partial v^2}{\partial x_j} \right] = \rho k f_{22} - 6\rho v^2 \frac{\varepsilon}{k} \quad (13)$$

The f_{22} equation is

$$L^2 \nabla^2 f_{22} - f_{22} = \frac{1 - C_1}{T_s} \left(\frac{2}{3} - \frac{v^2}{k} \right) - C_2 \frac{\mu_t 2S_{ij} \frac{\partial \bar{u}_i}{\partial x_j}}{\rho k} - 5 \frac{v^2/k}{T_s} \quad (14)$$

with

$$L = C_L \sqrt{\max \left(\frac{k^3}{\varepsilon^2}, C_\eta^2 \left(\frac{v^3}{\varepsilon} \right)^{1/2} \right)} \quad (15)$$

$$T_s = \max \left[\frac{k}{\varepsilon}, C_{kT} \left(\frac{v}{\varepsilon} \right)^{1/2} \right] \quad (16)$$

$$\mu_t = \rho C_\mu v^2 T_s \quad (17)$$

$$C_{\varepsilon_1}^z = 1 + 0.045 \sqrt{k/v^2} \quad (18)$$

A complete description of the V2F model can be found in [21].

LES (Large Eddy Simulation)

In a turbulent flow it is possible to make a distinction between the turbulent structures, or eddies, according to their size. The largest eddies extract kinetic energy from the mean flow field. Their size is in the order of the geometry and its time scale in the order of the mean flow, consequently to assume them as isotropic is a coarse simplification. There is an energy transfer from large eddies to smaller and smaller ones. In this cascade it becomes more and more difficult to distinguish the turbulent structures and the isotropic assumption becomes more representative. In the smallest eddies the energy is dissipated by viscous effects and goes to increment the flow's internal energy (heat).

The basic idea behind LES models is to resolve the largest turbulent scales. Consequently, it is necessary to run a three-dimensional, time-dependent computation with a mesh fine enough to capture the large eddies. Figure 5 is a good example of the resolution of large eddies. The effects of smaller eddies are accounted for with a sub-grid model. LES models differ in how the small eddies are modeled. In this work we use the Smagorinsky sub-grid model because it is the simplest and most commonly used.

The Navier-Stokes equations for the LES model are:

$$\frac{\partial \bar{u}_i}{\partial t} + \bar{u}_j \frac{\partial \bar{u}_i}{\partial x_j} = -\frac{1}{\rho} \frac{\partial \bar{p}}{\partial x_i} - \frac{\partial \tau_{ij}}{\partial x_j} \quad (19)$$

The convection term filtered out in the previous equation needs to be model. This is done with the sub-grid scales (SGS) stresses

$$\tau_{ij} = \bar{u}_i \bar{u}_j - \bar{u}_i \bar{u}_j \quad (20)$$

The Smagorinsky model defines

$$\tau_{ij} - \frac{1}{3} \tau_{kk} \delta_{ij} = -2C_{s2} \Delta^2 |\bar{S}| S_{ij} \quad (21)$$

with

$$\bar{S} = \sqrt{2S_{ij}S_{ij}} \quad (22)$$

where $\Delta = \text{cell volume}^{1/3}$ and C_{s2} is 0.165^2 .

Steady state modeling results and discussion

Every simulation is initialized with a zero velocity field and run with the first (1st) order upwind discretization scheme. Every simulation is run for a maximum of 4000 iterations. The convergence criterion is set to 1E-03 for all monitored residuals. The simulations satisfying the convergence criteria are further run with a second (2nd) order discretization scheme using as initial condition the flow field obtained with the 1st order simulations. “MARS” with 0.5 blending factor is used as 2nd order discretization scheme for all equations. These simulations are run for a maximum of 4000 iterations. This strategy is used to help convergence and allows for direct comparison between results obtained with 1st and 2nd order discretization schemes. The maximum run time for a simulation with such a convergence strategy is about 12h on 4 parallel nodes equipped with dual Intel Xeon X5460 (Quad-core, 3.16GHz).

The simulations generate a large amount of results. These are mainly summarized in diagrams, pictures and graphs. The results are discussed below, addressing the different parameters investigated. The first group of 54 simulations is run to allow cross evaluation over 5 parameters (turbulence model, mesh density, mesh topology, numerical discretization, Re). Based on the findings from the first group of simulations, a second, less extensive, group of simulations is run to further investigate the effects of mesh density and inlet velocity profile.

Effect of turbulence models

Figure 6 illustrates how the choice of turbulence model affects the results. Each subplot presents the results averaged in angular direction of 12 simulations (3 mesh densities, 2 mesh typology and 2 numerical discretization schemes). It is found that the turbulence model is the most important parameter. The k- ϵ model consistently over-predicts the heat transfer in the stagnation zone. It performs often well for $r/D > 2$ but it is inconsistent in this region where occasionally it under-predicts the experimental results. No clear explanation is found for this deviation. Figure 7 shows that k- ω is the most successful model in converging with a 2nd order discretization scheme. The k- ω model gives good agreement with experiments for small r/D (< 1.5) but deviates for greater r/D (see Figure 6).

The V2F model seems to be insensitive to all parameters (discretization scheme, mesh density and topology) as can be seen in Figure 6. It displays a more constant offset from the experimental data for all r/D , somehow under-estimating the experimental results. The spreading in the range $1 < r/D < 2$ occurs for simulations with the finest mesh and 2nd order discretization scheme. This spreading derives from the fact that the solution is not fully axisymmetric. Transient turbulent phenomena could be a cause of this effect. Figure 7 shows that the V2F model hardly reaches convergence with the 2nd order discretization scheme, however, the net average difference in Nu between solutions obtained with 1st and 2nd order discretization schemes is below 3.3%. This gives confidence on the successfulness of V2F. In other words, a solution obtained with the V2F model and the 1st order discretization scheme proves to be better than one obtained using the k- ϵ or k- ω model with the 2nd order discretization scheme.

A peak in convergence successfulness is reported for a mesh size of 0.5E06 cells (see Figure 7). A possible explanation is that coarser meshes are unable to resolve the flow features correctly. Finer meshes, on the other hand, fail to converge to a steady solution because of the inherently transient phenomena. Moreover, finer meshes generally need more iterations to converge.

Out of the first group of simulations, 87% converged using the 1st order numerical discretization scheme; of these, 50% further converged using the 2nd order scheme. In general, the residuals' plot for the non-converged simulations showed a stable cyclic fluctuation. This effect is often found when applying a steady state CFD approach to flows characterized by transient phenomena.

Effect of numerical discretization

The net average difference in Nusselt number between 1st and 2nd order discretization scheme is at maximum 3.8% for all simulation here considered. Solutions using a 2nd order scheme are more accurate than 1st order ones and always recommended. However, solutions achieved with 1st order discretization scheme can still be considered representative and be used if convergence with a 2nd order scheme is difficult to obtain. Given that the user has already found confidence in the model.

Figure 7 shows that the “peacock” topology is more successful than the “butterfly” one in reaching a converged solution with a 2nd order discretization scheme. Further analysis indicates that, on average, peacock meshes give results closer to experimental data.

Effect of Reynolds number

In impinging jets, heat transfer is strongly dependent on the Reynolds number. Figure 8 compares simulation results with experimental data for various Re at two different locations. Although the absolute values do not closely match the measured data, the main trend for Nu as function of Re at $r/D=0$ is captured by all turbulence models. For larger r/D , results for the k- ϵ show a wide spreading deriving from a strong dependency on other parameters. The k- ω and V2F models present a more consistent offset from the experimental data.

Effect of mesh density and distribution

The selected group of cases used for the mesh independency study is defined by the following parameters: Re=20000, k- ϵ and V2F models, butterfly and peacock mesh topology, mesh density (0.25E06, 0.5E06, 1E06 and 2E06 cells). In general, no significant differences are found between the results obtained for meshes with more than 0.5E06 cells. The k- ϵ model presents significant difference between results obtained with 0.25E06 and 0.5E06 cells. The V2F model presents only minor differences between all the meshes tested. This indicates that the degree of mesh dependency varies with the turbulence models.

The study on mesh dependency is extended to consider the effect of mesh density in wall-normal direction with the meshes presented previously. For this study, the configuration of Re=23000 and H/D=6 with the V2F turbulence model and fully developed inlet boundary conditions is used. Results are shown in Figure 9. All meshes tested deliver good results, in particular mesh 1 matches the experimental result very well.

Effect of inlet velocity profile

The experimental data used for comparison in this work come from experiments performed with jets issued from a fully developed pipe flow, while all simulations presented above are performed with a uniform flow. Which is a common approach e.g. [13, 17]. Impinging jet heat transfer is a strong function of the Reynolds number and consequently of the flow momentum as can be seen in Figure 8. A fully developed velocity profile has a higher flow momentum in the jet's center compared to the corresponding uniform flow (i.e. for the same Re). This affects the impinging jet heat transfer.

Simulations are run to study the effect of inlet velocity profile with the following parameters: $Re=20000$, $k-\epsilon$ and V2F turbulence models, butterfly and peacock mesh topology, $0.5E06$ and $1E06$ mesh density. The applied velocity profile is obtained as described previously. The velocity at the pipe's center for the fully developed profile is about 1.23 times the velocity of a uniform flow profile (at $Re=20000$).

Results regarding the effect of the inlet velocity boundary profile are presented in Figure 10 (top). The results obtained with the fully developed inlet velocity profile and V2F model agree with the experimental results almost within the confidence interval of the data.

For $r/D < 2$ the effect of the inlet velocity profile is very important as shown in Figure 10 (top). For greater r/D the influence of the inlet conditions are negligible for $k-\epsilon$ while some effects are still noticeable for the simulations performed with the V2F model. Note the inconsistency of the $k-\epsilon$ model mentioned before referring to Figure 6.

With the fully developed inlet profile the jet has higher core velocity and this is retained farther downstream the nozzle. Consequently, the jet is more compact and concentrates on a smaller surface, resulting in a higher heat transfer coefficient in the impingement zone Figure 10 (bottom). The results obtained with the fully developed inlet velocity match the experimental results quite well, including the location and magnitude of the secondary peak.

Figure 10 (bottom) shows data from all wall cells (i.e. not averaged in angular direction). The data scatter in the region $1 < r/D < 3$ results from the fact that the solution is not perfectly axisymmetric. Important transient phenomena are expected in this area. Moreover, this study shows a relatively low convergence success (about 50% considering all simulations). These facts suggest that a representative axisymmetric steady state solution is difficult to achieve and that a transient simulation might be more appropriate.

Conclusions for RANS (steady state) approach

This part of the work has extensively studied the case of an impinging jet at $H/D=2$ with a steady state approach. The V2F performs best as a turbulence model. The peacock mesh topology gives the best results both with respect to convergence, robustness and accuracy. Finer meshes give better results, but show more frequently convergence problems. 2nd order numerical discretization gives results slightly closer to experimental data than 1st order, but more often encounters convergence problems. For all cases, the choice of turbulence model has a much stronger influence than other variables (e.g.

discretization order or mesh density). Moreover, the way in which mesh independency is affected by the turbulence model is discussed. The inlet velocity profile has a significant influence on simulation results. A uniform velocity profile cannot be used to represent a fully developed velocity profile in these types of flows.

Two facts suggest that important transient effects prevent the simulation from reaching a converged steady state solution.

- The use of finer mesh and higher numerical discretization order often leads to non-axisymmetric solutions but better agreement with the experimental data.
- Relatively low convergence success is found due to cyclic oscillation of the residuals.

Significant transient phenomena are also measured by [6] and pointed out as an explanation for the peculiarity of impinging jet flows. For these reasons RANS simulations might not be capable of capturing the physics at play.

Transient modeling results and discussion

All simulations are run for 200s (simulated time) and the averaging for post-processing is done on the last 100s. The statistical relevance of this average is checked with cases run for a longer period. The quantities describing the turbulence in the jet flow are normalized with the jet bulk velocity at the nozzle outlet W_b . The discussion regards LES and mesh 3 unless otherwise stated.

Effects of the numerical discretization

Three cases are run with values for the MARS parameter of 0, 0.25 and 0.5. A low value for the MARS parameter dampens the resolved turbulence fluctuations with a clear trend particularly for $w'w'$ at $r/D=0$ (see Figure 11 top). On the other hand no sensible difference or trend is appreciated on the average Nu (Figure 11 bottom).

In the literature, use of the CD scheme is recommended for LES simulations at least for the momentum equations. A few attempts to apply this scheme gave no good results generating unphysical values for the Nu number. MARS 0.25 is used as default value to enhance the likelihood of achieving convergence.

Effect of inlet turbulence

Cases are run respectively with halved and doubled inlet synthetic turbulent fluctuations, corresponding to 25% and 400% of the nominal value for k at the inlet. A rapid decrease in resolved k is observed close to the inlet for $r/D=0$ (Figure 12 top). For $r/D=0.5$ (i.e. nozzle edge) the turbulent fluctuations grow very rapidly with the resolved turbulence growing up to one order of magnitude compared to the values imposed at the inlet. This effect largely overcomes the inlet turbulence at $r/D=0$ when the shear layer reaches the jet center at about $z/D=3$. A similar effect can be noticed at $r/D=1$ where the resolved turbulence is negligible until the shear layer effects are felt at about $z/D=2.5$. Consequently the inlet turbulence level has little effects on the average Nu number. Only small differences at $r/D=0$ follow the trend for growing inlet turbulence (Figure 13). Farther away from the impingement point, the simulation results closely follow experimental data.

The behavior described above is confirmed by the plots of specific velocity fluctuations (Figure 12 bottom). Inlet synthetic fluctuations have appreciable effects only in the potential core $r/D=0$ where the case with nominal values of turbulence ($k_{in}=100\%$) best matches the experimental results both magnitude and shape.

Mesh size effects

Three meshes are tested with the LES model with a similar number of cells but different distribution in wall-normal direction (mesh 1, mesh 2 and mesh 3 described in Table 1).

Figure 14 (top) shows the effect of cell size on the turbulent fluctuations near the inlet. Mesh 1 has larger, more elongated, cells close to the inlet and results in an evident dampening effect on the turbulent fluctuations. For all meshes there is a rapid decrease in velocity fluctuations along the flow's direction for $r/D=0$. With mesh 1 the velocity fluctuations in the shear layer ($r/D=0.5$ Figure 14 top (b)) develop slower but eventually reach values very similar to the ones obtained with the other meshes at about $z/D=1$.

The difference between the three meshes in the near wall region is remarkable. All meshes are identical for $z/D < 0.5$ and have similar values for the turbulent variables for $z/D > 0.5$ (see for example Figure 14). Yet the three meshes behave in a considerably different manner approaching the wall. Only mesh 3 shows a rapid decrease in velocity fluctuations approaching the wall, which is the expected behavior for a low Re model (Figure 14 bottom).

The heat transfer prediction for the simulations run with the LES approach are plotted in Figure 15 (top). All meshes give results relatively close to the experiments, with up to about 25% local deviation. It can also be observed that the results are fairly parallel to each other. Interestingly, there is no trend correlation between Nu and the magnitude of fluctuation close to the wall (for example, compare Figure 14 (bottom) and Figure 15 (top) at $r/D=1$).

URANS models are also tested with different wall-normal cell distribution. The remarkable result is that URANS models fail completely to predict the wall heat transfer using mesh 2, but work well with mesh 1. A number of tests are conducted to identify the cause of this behavior. The same models are tested in their RANS implementation (steady state) and give results very close to the experiments with all meshes (see Figure 15 bottom).

Further analysis reveals a correlation between the flow's turbulent quantities and the predicted heat transfer. As an example, Figure 16 (bottom) shows the development of μ_t (turbulent dynamic viscosity) at different locations. Here it is possible to note that they behave similarly to the LES model where, for mesh 2, turbulent quantities do not tend to zero approaching the wall. Notably, in the LES case the heat transfer prediction is satisfactory, while the URANS models give unphysical results.

A possible explanation for the strong dependence of URANS models (k- ϵ and V2F) on the mesh wall-normal spacing, could be as follows: if the mesh size is coarse near the inlet (mesh 1), fluctuations are not resolved and the model behaves essentially in RANS mode (see Figure 16 top). If instead the mesh is fine enough (mesh 2), a larger part of the velocity fluctuations u' is resolved. Consequently higher velocity gradients are present in the flow and this increases the value of the strain tensor S_{ij} . This variable is active in the production term, P_k , of the k transport equation, which, in turns, increases the value of μ_t as shown in Figure 16 (bottom).

Although high, μ_t in the V2F model does not manage to sufficiently damp the velocity fluctuations approaching the wall; consequently, the model fails to predict the heat transfer. The standard k- ϵ (not realizable) generates higher μ_t than the V2F model which effectively dampens velocity fluctuations approaching the wall. This behavior is confirmed by comparing the development of μ_t for RANS and URANS (Figure 16 bottom). Indeed, in the RANS case no fluctuations are resolved by definition and both mesh 1 and 2 bring heat transfer prediction close to the experimental data (Figure 15 bottom).

The effect of mesh density in wall-parallel direction on the Nu number for the transient k- ϵ and V2F model can be seen in Figure 17. Three different meshes are tested with 0.125E6, 0.5E6 and 2E6 cells, these are obtained refining the coarsest mesh in an angular

and radial direction. Mesh 1 is used as reference for wall-normal spacing. The V2F model gives results close to the experimental data. It can be seen that the Nu number slightly increases with increasing cell density, driving results with the k- ϵ model farther away from experimental data. One could argue that mesh independency has not been reached. Another possible explanation is that mesh resolution is too fine for the k- ϵ model to work properly as URANS.

Effect of nozzle to wall distance

An LES simulation is run for the case of nozzle to wall distance $H/D=2$. The simulation is based on a mesh obtained chopping mesh 3 at $z/D=2$, resulting in a total of $1.6E6$ cells. The predicted Nu number for $H/D=2$ is very similar to the $H/D=6$ case with noticeable differences only for $r/D < 0.5$ (Figure 18 top). These are probably related to the limited interaction of the shear layer with the potential core for $H/D=2$, as can be seen in Figure 18 (bottom). Furthermore, comparing simulation results with the experimental data in Figure 18 (top), it is noticeable that the simulation for $H/D=2$ does not capture the secondary peak characteristic of this jet configuration.

Computational cost

Figure 19 plots the time necessary for one CPU to compute one second of simulated time. This time is affected by many factors such as the number and type of CPUs used. Another important factor is the need to solve extra subroutines. These are for example the two extra subroutines used for the implementation and post processing of the synthetic fluctuation. In parallel computing, communication between CPUs is a significantly time-consuming process. The domain is partitioned in groups of cells and each group is assigned to a CPU. At the end of each iteration, the solution at the group's boundaries needs to be passed to the CPU(s) computing for the adjacent group.

For the reasons presented above, the data from Figure 19 can be treated only as indicative. It can be noticed that the V2F is slightly slower than the k- ϵ model. This is probably due to the fact that the V2F model solves for two extra equations. Nine simulations run the LES model with the same CPU configuration. The standard deviation for the runtime of these simulations is about 11%. In Figure 19 the computational cost related to the growing number of cells can also be appreciated. Computation time for steady state simulations is shown for comparison.

Conclusions for transient approach (LES, URANS)

The URANS models are found to be very sensitive to the mesh wall-normal distribution. For most meshes tried, URANS models act much like their respective steady state simulation. In these cases, the k- ϵ model is verified to be not sufficiently accurate in predicting heat transfer in the impingement zone. The V2F model is slightly more computationally expensive but gives significantly better results, even with a relatively coarse mesh. On the other hand the V2F model is more likely to diverge. If the mesh is sufficiently fine, the URANS models can resolve a significant part of the turbulent fluctuations. In this case, it is shown that the k- ϵ model is more effective in dampening the velocity fluctuations than the V2F model. However, as discussed previously, both models fail to give a worthy prediction of the heat transfer.

The LES model is studied more extensively, changing a number of parameters. This model is capable of resolving the turbulent structures in the shear layer in a satisfactory manner. The results are good both in terms of heat transfer prediction and flow-field turbulent characteristics. Only relatively little differences are noted when changing the various parameters. The LES model is also found to be sensitive to the wall-normal cell distribution. The most remarkable effects of this are seen on the resolved velocity fluctuations in the near wall region. Unfortunately, LES simulations are inherently expensive, since it requires both a fine mesh and a transient simulation, exponentially increasing the computational cost.

Using the LES model allows to study the effect of inlet turbulent fluctuations. These are found to be significantly smaller than the turbulence produced in the shear layer. For nozzle to wall spacing $H/D=6$, the shear layer has enough space to spread into the potential core. Consequently, inlet fluctuations play only a minor role in the heat transfer at the impingement point.

Conclusions

The objective of this work is to evaluate different approaches to the simulations of impinging jet flows. The test and cross-evaluation of many different models is useful when deciding how to address modeling this kind of flow. Here, two major approaches are extensively tested, steady state and transient, for which specific conclusions are reported at the end of the respective sections. With both approaches it is possible to reach a useful results, a careful simulation setup is however necessary. The choice of the best approach is therefore determine by the level of accuracy necessary for the results and the available computational resources.

References

1. Baughn, J. W. and Shimizu, S. [1989], Heat transfer measurements from a surface with uniform heat flux and an impinging jet, ASME J. Heat Transfer 111/1097.
2. Katti, V. and Prabhu, S.V. [2008], Experimental study and theoretical analysis of local heat transfer distribution between smooth flat surface and impinging air jet from a circular straight pipe nozzle, Int. J. Heat Mass Transfer article in press.
3. Lytle, D. and Webb, B.W. [1994], Air jet impingement heat transfer at low nozzle plate spacings, Int. J. Heat Mass Transfer 37 1687–1697.
4. Gao, N., Sun H. and D. Ewing [2003], Heat transfer to impinging round jets with triangular tabs, Int. J. Heat Mass Transfer 46 2557–2569.
5. O'Donovan T. S. and Murray D. B. [2007], Jet impingement heat transfer – Part I: Mean and root-mean-square heat transfer and velocity distributions, Int. J. Heat and Mass Transfer 50 3291–3301.
6. O'Donovan T. S. and Murray D. B. [2007], Jet impingement heat transfer – Part II: A temporal investigation of heat transfer and local fluid velocities, Int. J. Heat and Mass Transfer 50 3302–3314.
7. Yue-Tzu Yang, Shiang-Yi Tsai [2007], Numerical study of transient conjugate heat transfer of a turbulent impinging jet. Heat and Mass Transfer 50 799–807.
8. Gao N. and Ewing D. [2006], Investigation of the effect of confinement on the heat transfer to round impinging jets exiting a long pipe, Int. J. of Heat and Fluid Flow 27 33–41
9. Koseoglu M.F. and Baskaya S. [2007], The effect of flow field and turbulence on heat transfer characteristics of confined circular and elliptic impinging jets, Int. J. of Thermal Sciences article in press.
10. Viskanta R. [1993], Heat transfer to impinging isothermal gas and flame jets. Experimental Thermal and Fluid Science 6:111-134
11. K. Jambunathan, E. Lai, M. A. Moss and B. L. Button [1992], A review of heat transfer data for single circular jet impingement, Int. J. Heat and Fluid Flow, Vol. 13, No. 2 106-115
12. L. Davidson [2007], Using isotropic synthetic fluctuations as inlet boundary conditions for unsteady simulations. Advances and applications in Fluid Mechanics, Vol. 1 Issue 1 1 - 35
13. Lien, F.S., Chen, W.L. and Leschziner, M.A. [1996], Low-Reynolds-Number Eddy-Viscosity Modelling Based on Non-linear Stress-Strain/Vorticity Relations, Proc. 3rd Symp. on Engineering Turbulence Modelling and Measurements, Crete, Greece.

14. M. Angioletti, E. Nino, G. Ruocob. [2005], CFD turbulent modelling of jet impingement and its validation by particle image velocimetry and mass transfer measurements, *International Journal of Thermal Sciences* 44 349–356
15. M. Bovo, S. Etemad, L. Davidson. [2009], On the numerical modeling of impinging jet heat transfer, *Int. Symp. on Convective Heat and Mass Transfer in Sustainable Energy*, Tunisia
16. Cooper, D., Jackson, D. C., Launder, B. E. & Liao, G. X. [1993], Impinging jet studies for turbulence model assessment-I. Flow-field experiments. *Int. J. Heat Mass Transf.* 36, 2675–2684.
17. H. M. Hofmann, R. Kaiser, M. Kind, H. Martin. [2007], Calculations of steady and pulsating impinging jets—an assessment of 13 widely used turbulence models, *Numerical heat transfer, part b*, 51: 565–583.
18. Thomas Hällqvist. [2006], Large Eddy Simulation of Impinging Jets with Heat Transfer KTH Mechanics, SE-100 44 Stockholm, Sweden, dissertation thesis.
19. Tobias Husberg, Savo Gjiria and Ingemar Denbratt. [2005], Piston Temperature Measurements by use of thermographic phosphors and thermocouples in a heavy-duty diesel engine run under partially premixed conditions, SAE 2005-01-1646.
20. J. O. Hinze. [1975], *Turbulence*, McGraw-Hill
21. Durbin, P.A. [1995], ‘Separated flow computations with the k - ϵ - v^2 model’, *AIAA Journal*, 33(4), pp. 659–664.
22. Wilcox, D.C. [1998], “Turbulence Modelling for CFD”. 2nd edition, DCW Industries, Inc.

Tables

Table 1 Mesh size values in wall normal direction

	Mesh 1	Mesh 2	Mesh 3
Total cell nr	2E6	2E6	2.4E6
Number of layers	100	100	123
Near wall cell size	3.6E-3 D	3.6E-3 D	3.6E-3 D
Near inlet cell size	0.18	0.05	0.05
Growth ratio switch	None	0.5	2
Near wall / switch / till top	1.06	1.06 / 2 / 1	1.06 / 1 / 1

Table 2 Coefficients for the k- ϵ turbulence model

C_μ	σ_k	σ_ϵ	$C_{\epsilon 1}$	$C_{\epsilon 2}$	$C_{\epsilon 4}$
0.09	0.75	1.15	1.15	1.9	-0.33

Table 3 Coefficients for the V2F turbulence model

C_μ	$C_{\epsilon 3}$	α	β_0	β_0^*	σ_k^ω	σ_ω^ω
0.09	1.44	0.52	0.072	0.09	2.0	2.0

Table 4 Coefficients for the V2F turbulence model

C_μ	σ_k	σ_ϵ	$C_{\epsilon 1}$	$C_{\epsilon 2}$	C_1	C_2	C_L	C_η	C_{kT}
0.22	1.0	1.3	1.4	1.9	1.4	0.3	0.23	70.0	6.0

Figures

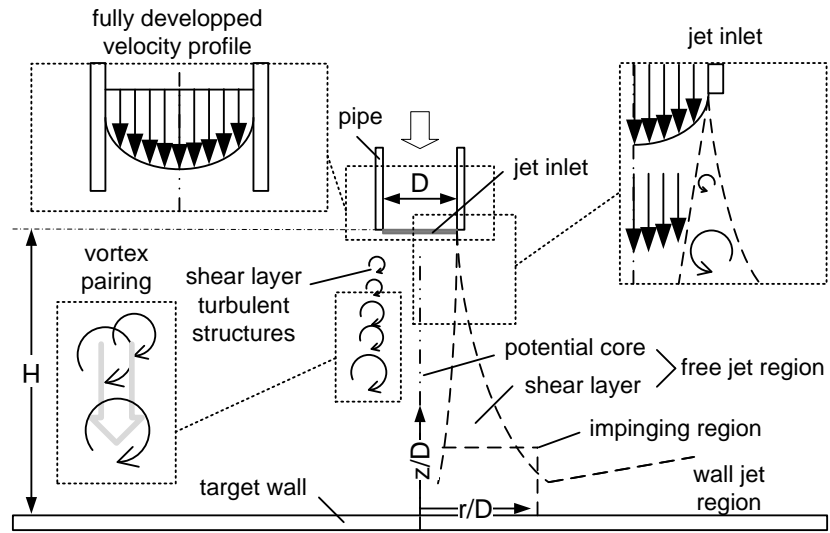


Figure 1. Physical processes in impinging jets.

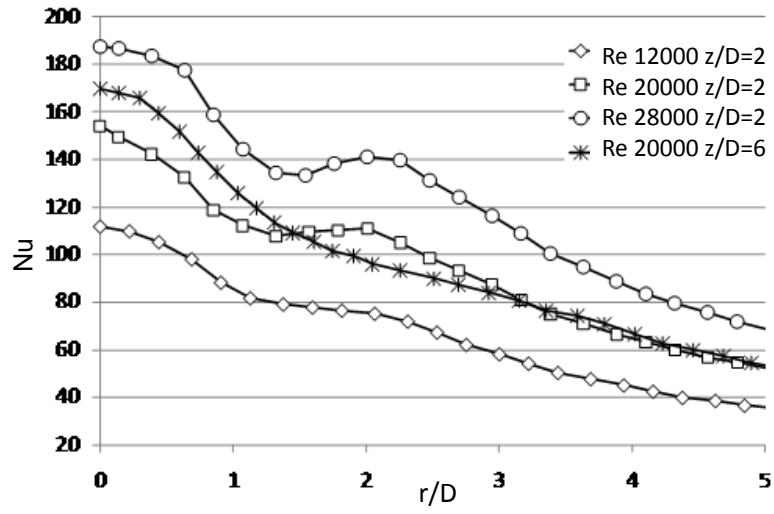


Figure 2. Experimental results $Nu(r/D)$ [2].

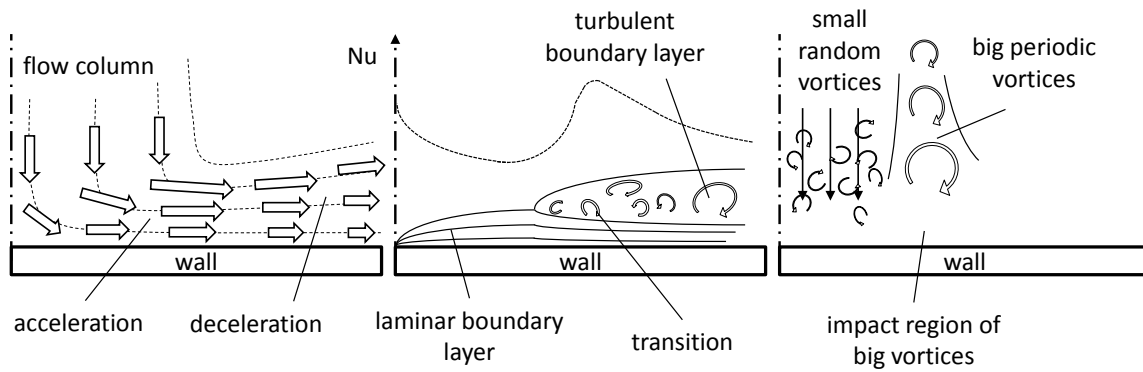


Figure 3. Qualitative representation of near wall impinging jet flow. (left) acceleration-deceleration effect. (center) flat plate boundary layer development and related heat transfer. (right) shear layer vortices impact region.

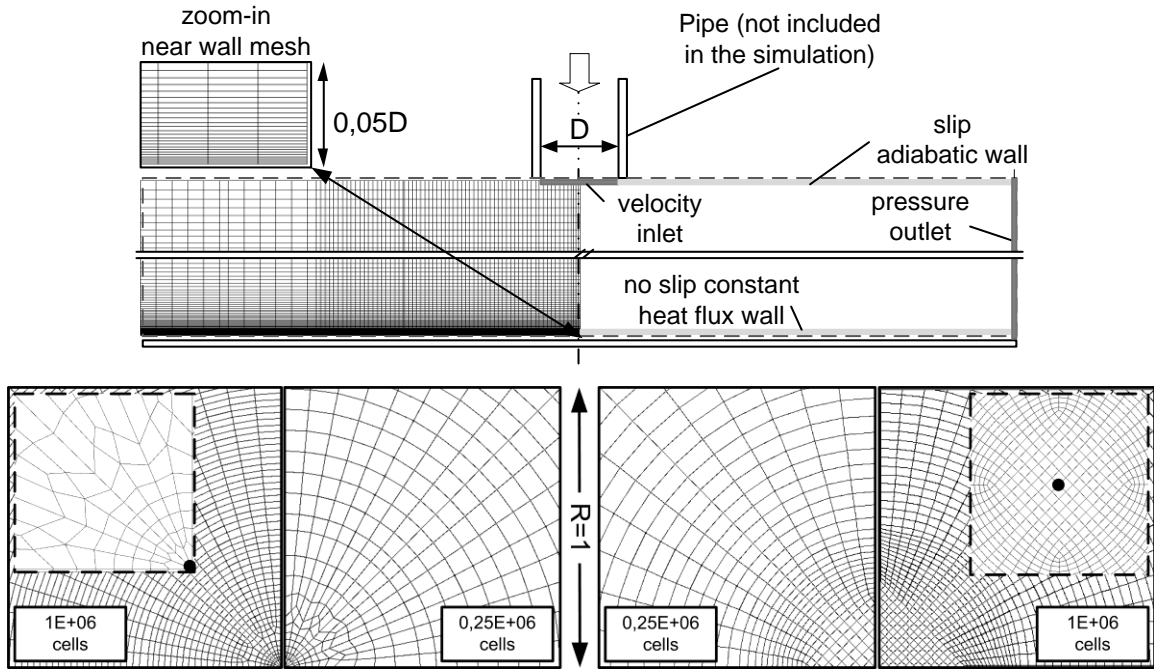


Figure 4. (top) Computational domain, mesh and boundary conditions. (bottom) Peacock (left) and Butterfly (right) mesh topology. The black dot in the zoomed images represents the mesh center.

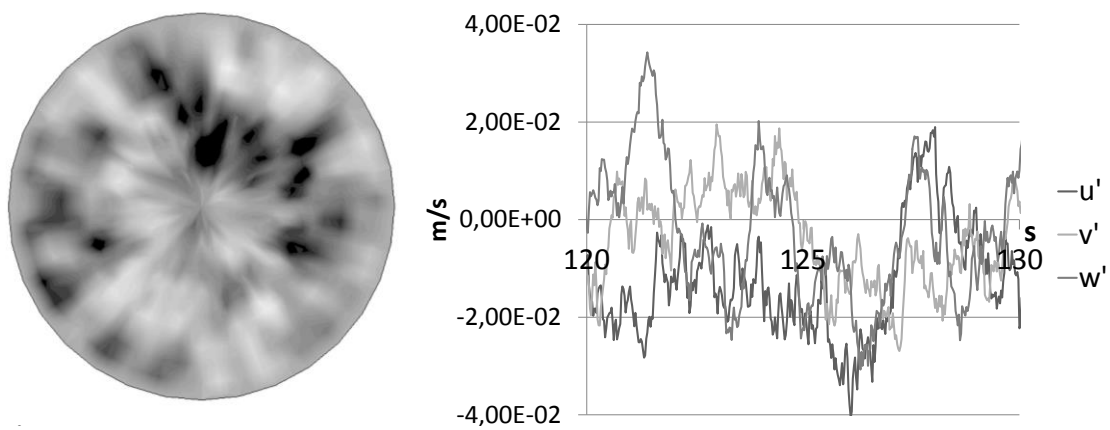


Figure 5. Example of synthetic fluctuations superimposed at the inlet. Instantaneous inlet u' field and time resolved fluctuations in one inlet boundary cell.

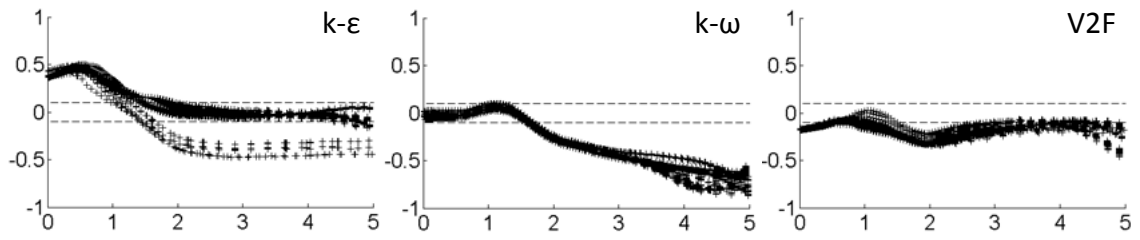


Figure 6. Normalized difference between simulation results and experimental data for $Re=20000$ as function of r/D . Experimental results from Baughn and Shimizu [1] and Katti and Prabhu [2]. The ± 0.1 stripe represents 10% deviation from the average of the two experimental sets.

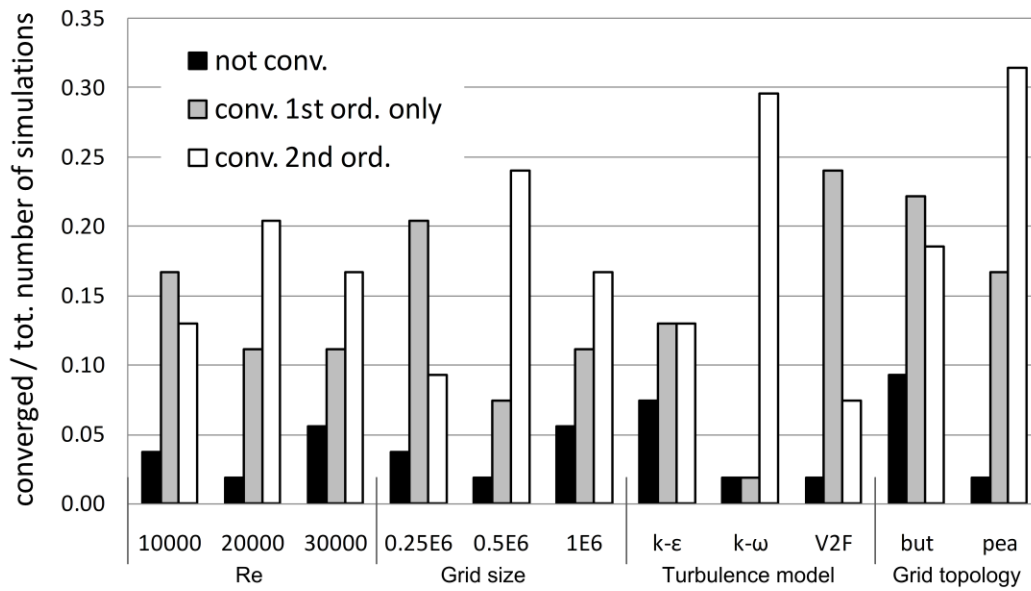


Figure 7. Convergence success relative to parameter (but = butterfly and pea = peacock).

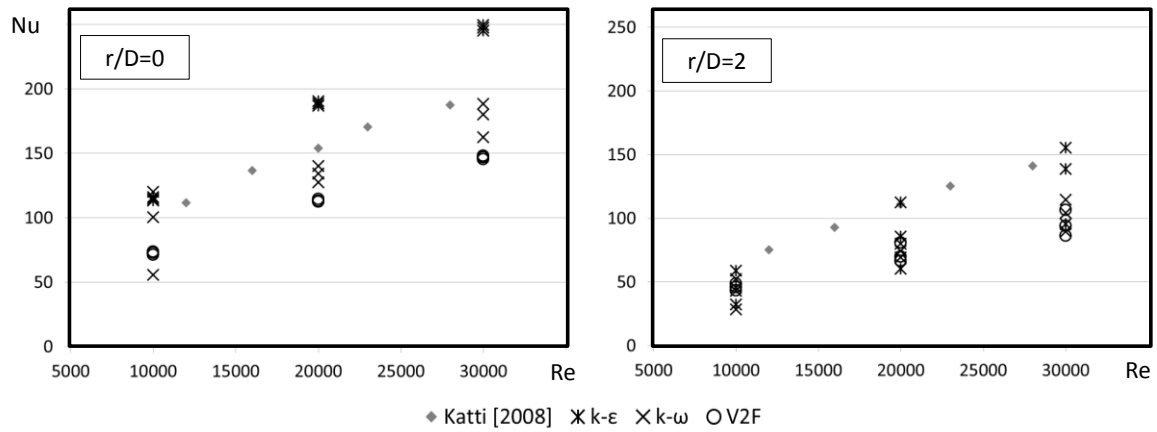


Figure 8. Effect of Re on the Nu at $r/D=0$ (stagnation point) and $r/D=2$. Experimental data from Katti and Prabhu [2]. For each turbulence model 3 values are presented: average, maximum and minimum. Note that their difference might be within graphical resolution (i.e. they overlap).

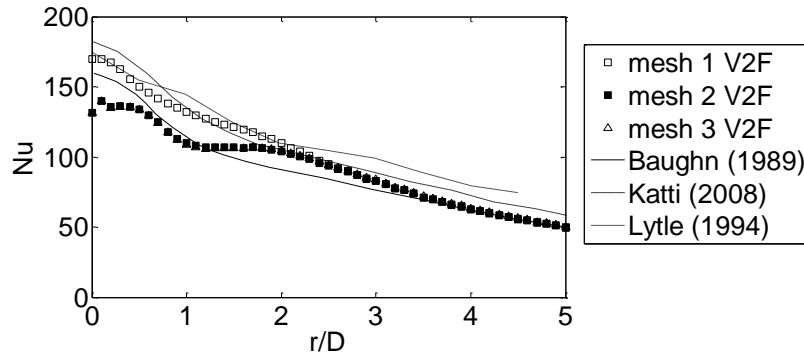


Figure 9. Effect of wall-normal mesh density on the Nu.

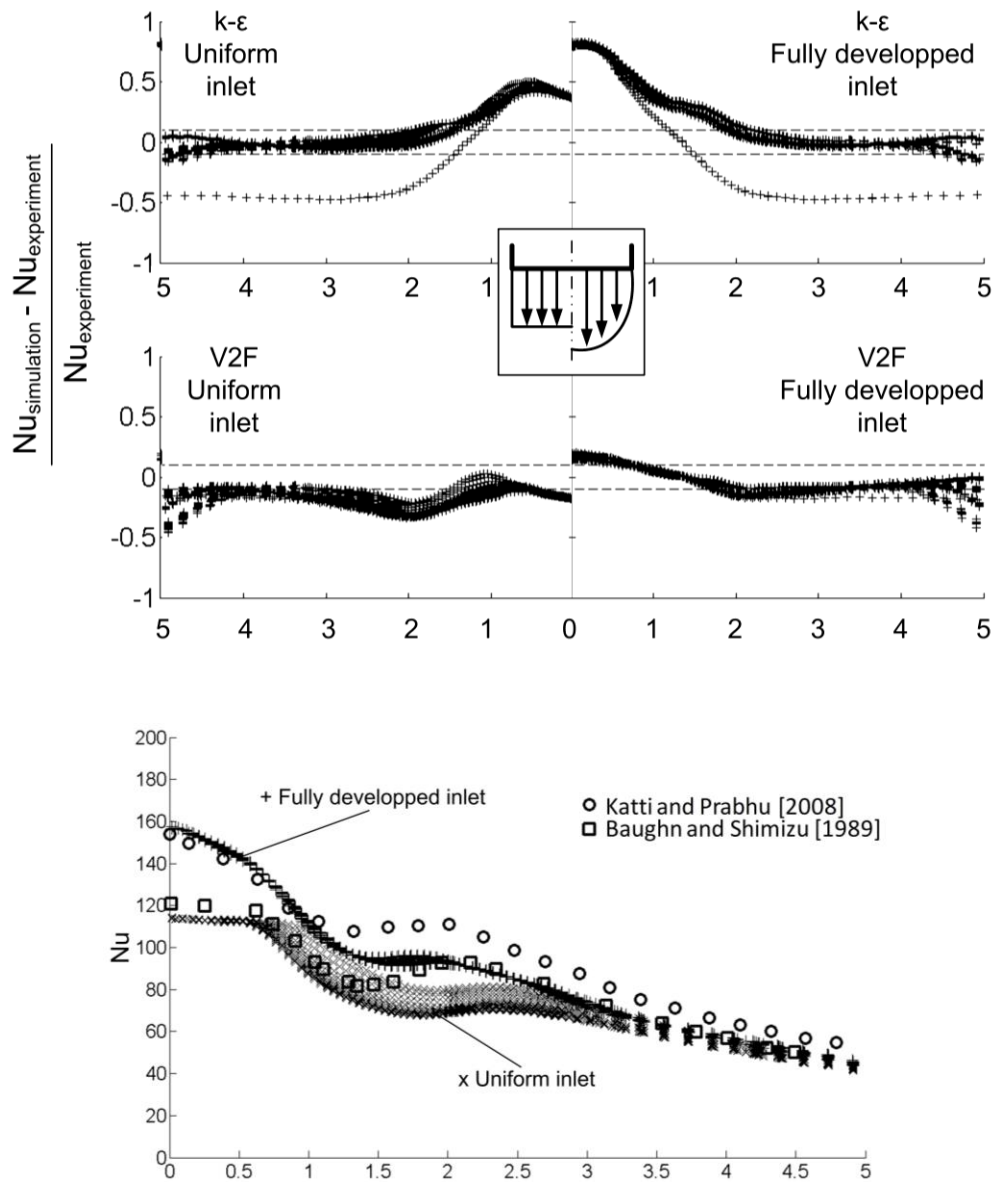


Figure 10. (top) Effect of inlet velocity profile. Simulation results for $Re=20000$, mesh density $0.5E06$ and $1E06$, butterfly and peacock mesh topology. Comparison with experimental results from Baughn and Shimizu [1] and Katti and Prabhu [2]. (bottom). $Nu(r/D)$ comparison between results with the V2F model and experiments at $Re=20000$. Numerical simulation parameters (V2F turbulence model, $0.5E06$ mesh cells, peacock topology, 2^{nd} order discretization scheme).

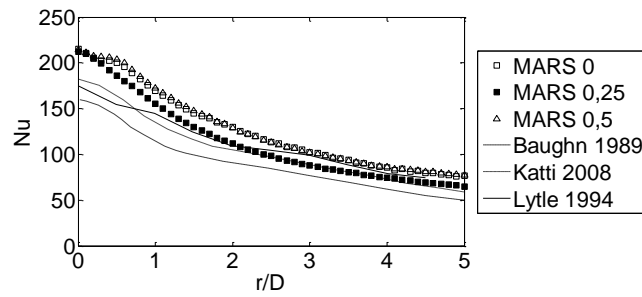
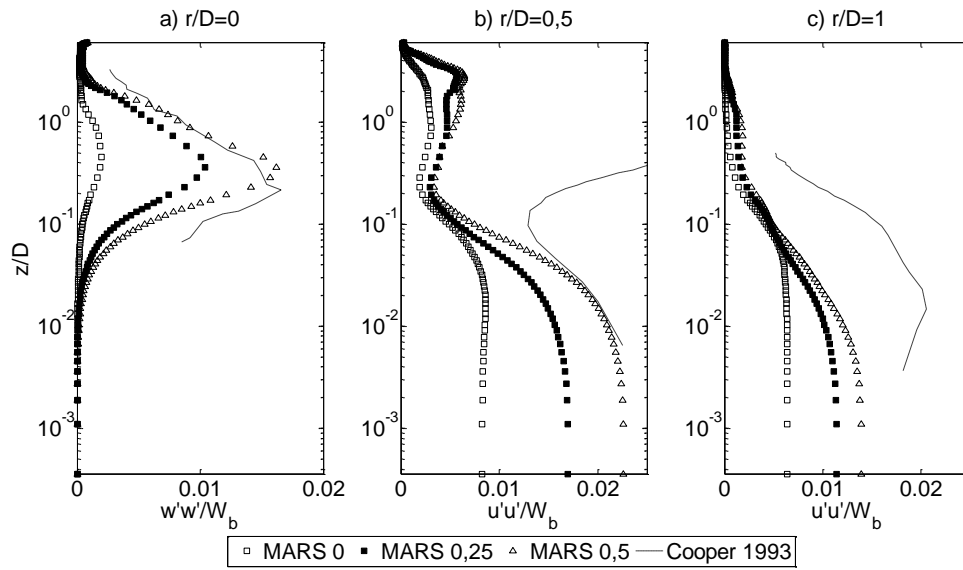


Figure 11. (top) Effects of differentiating scheme on velocity fluctuations. (bottom) Effect of differentiating scheme on Nu.

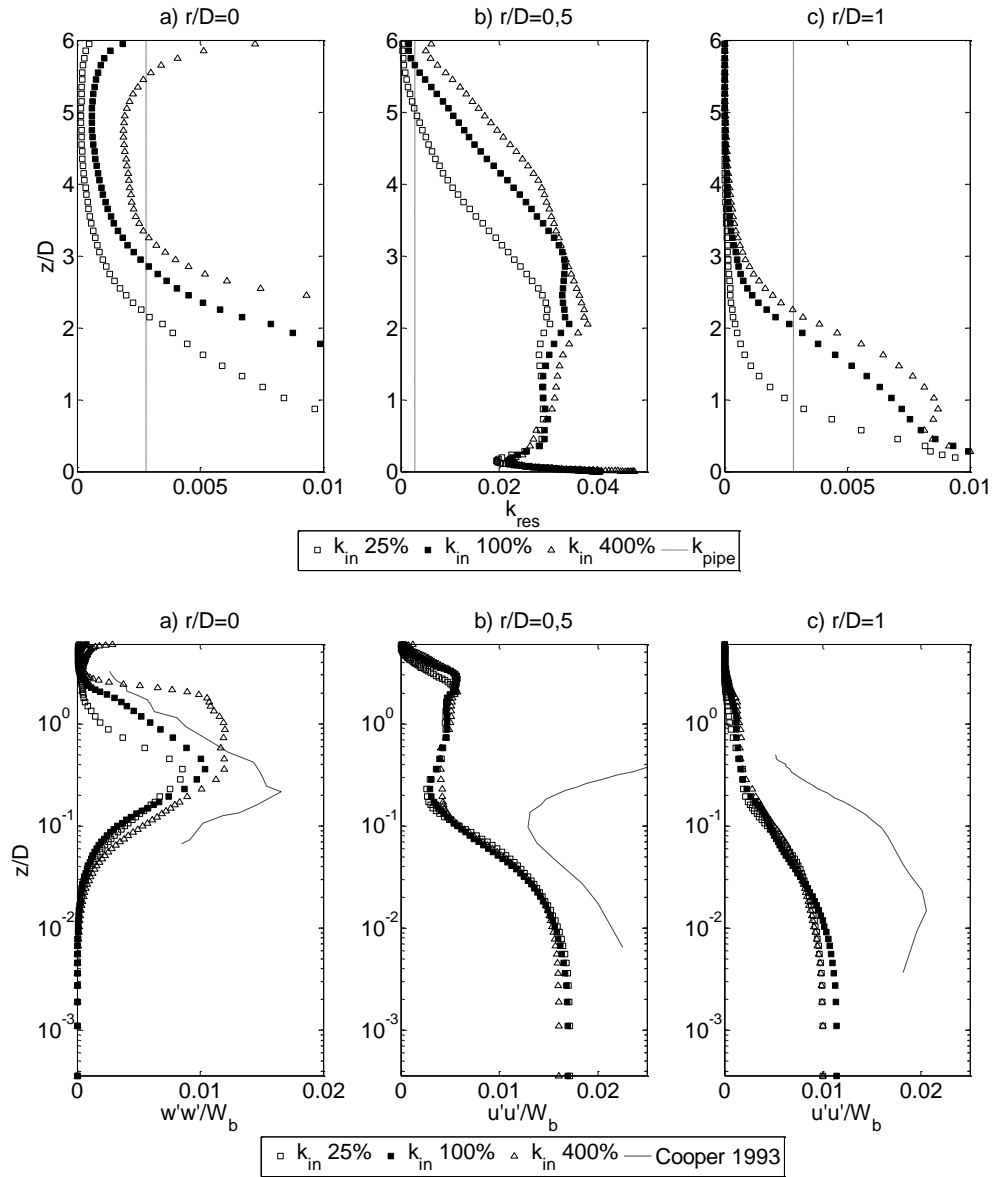


Figure 12. (top) Effects of inlet turbulence on resolved k (k_{res}). Fully developed pipe flow “ k_{pipe} ”. (bottom) Effects of inlet turbulence on resolved velocity fluctuations.

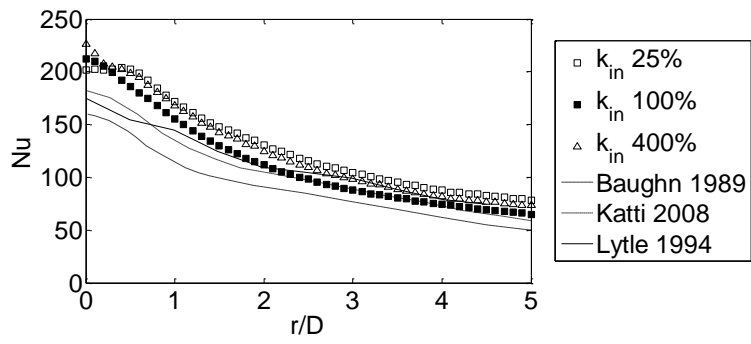


Figure 13. Effect of inlet turbulence on Nu.

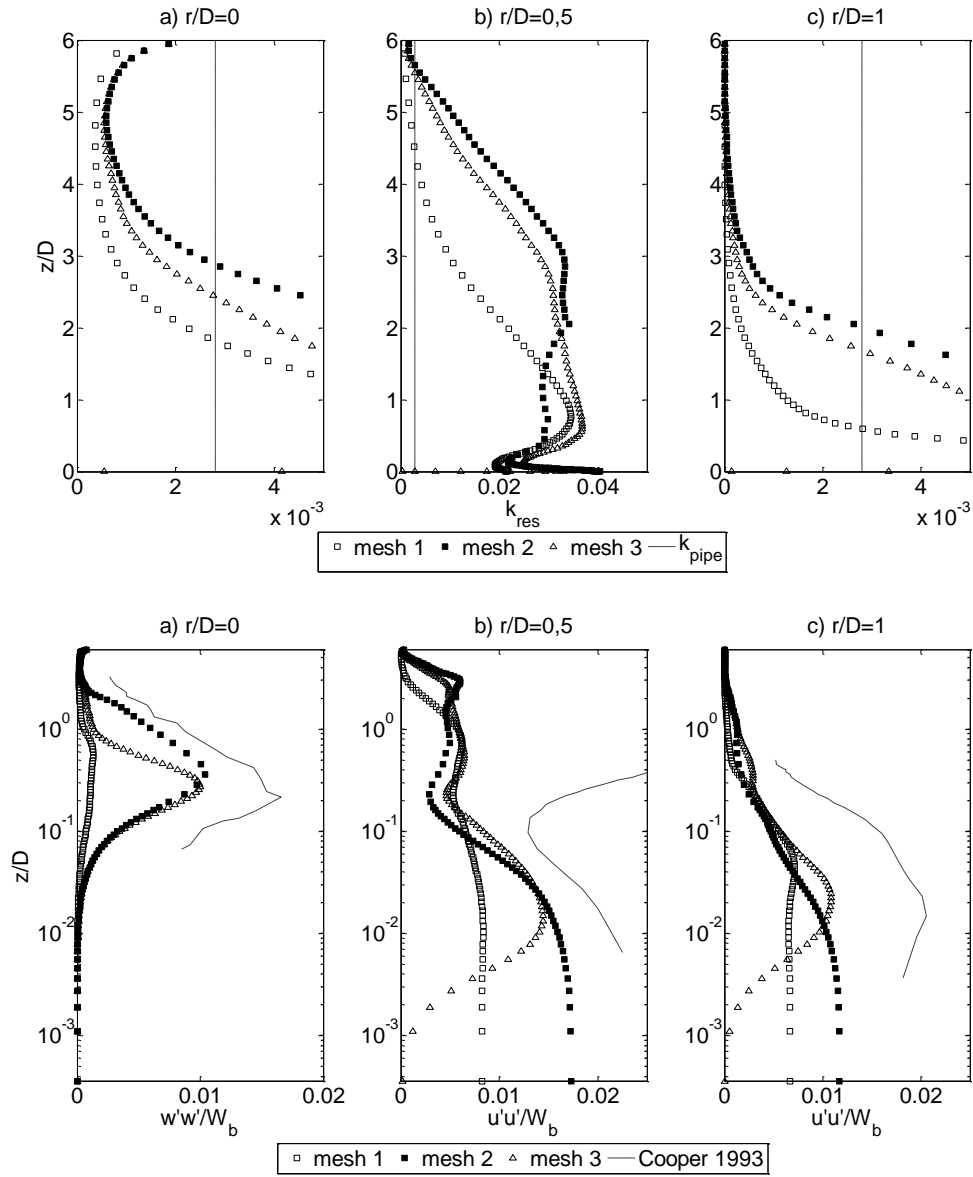


Figure 14. (top) Effects of wall-normal cell distribution on resolved k (k_{res}). For reference fully developed pipe flow “ k_{pipe} ”. (bottom) Effects of cell wall-normal distribution on resolved velocity fluctuations.

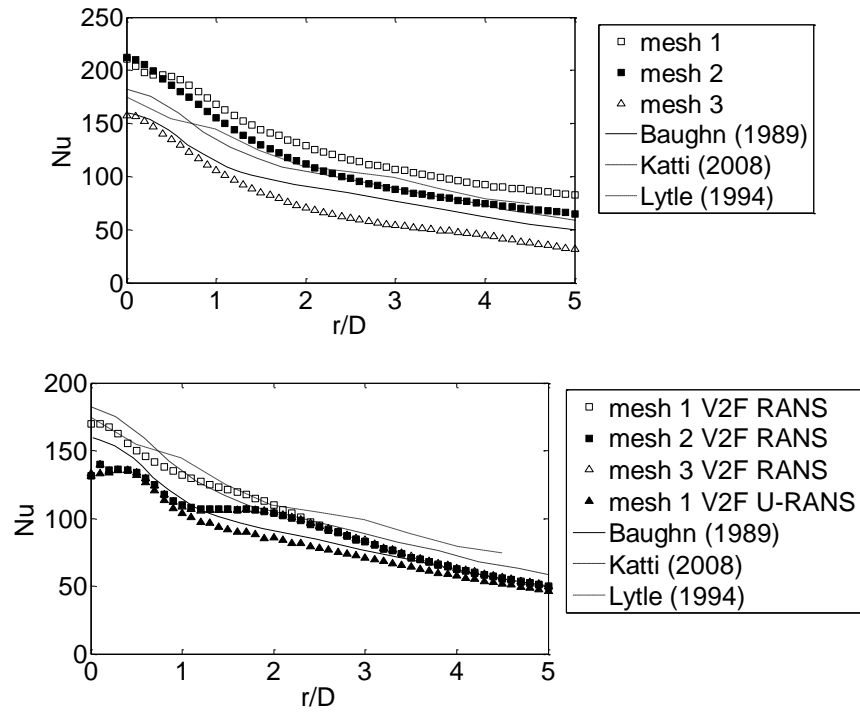


Figure 15. (top) Effect of wall-normal density distribution on Nu. (bottom) Comparison between RANS and URANS.

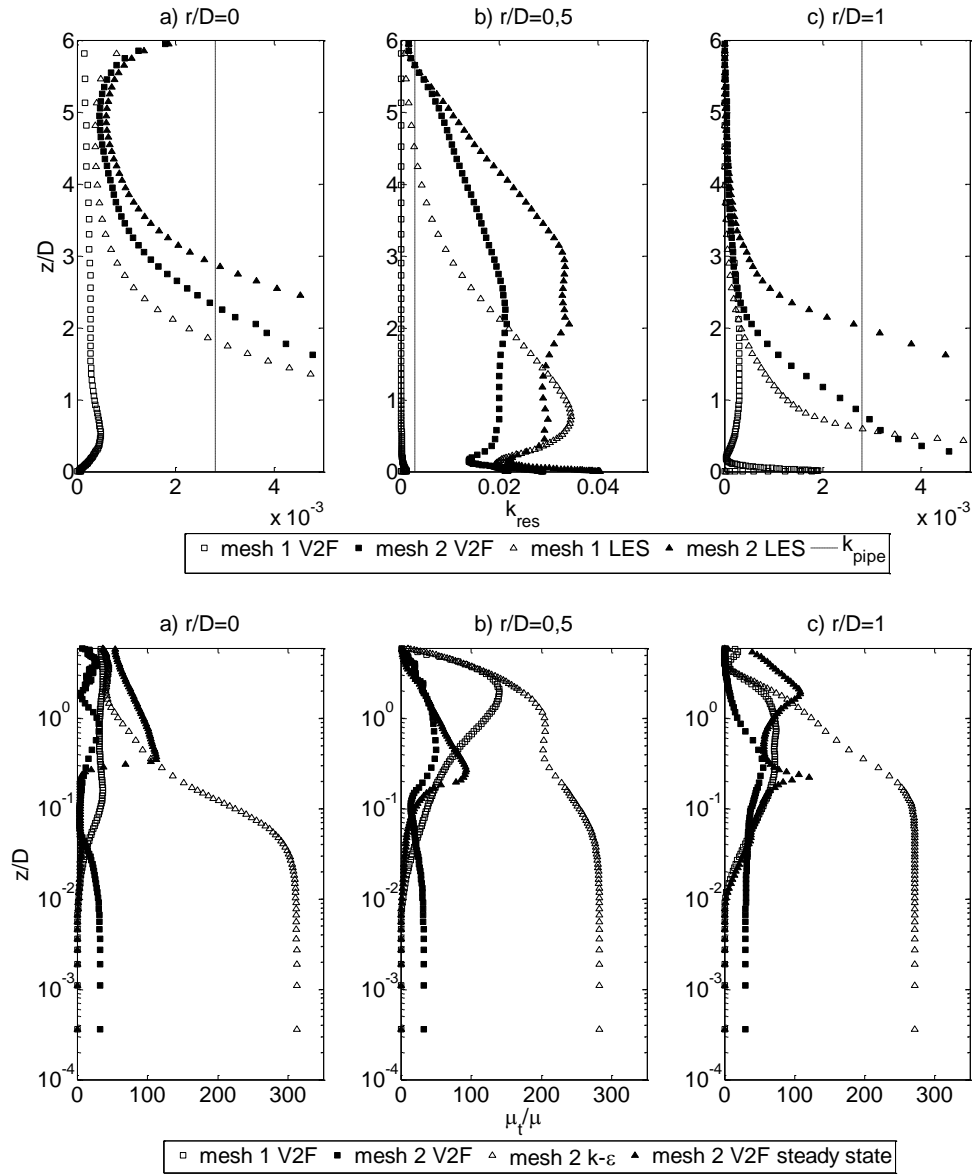


Figure 16. (top) Mesh and turbulence model effects on resolved k (k_{res}). (bottom) μ_t development for URANS and RANS (steady state).

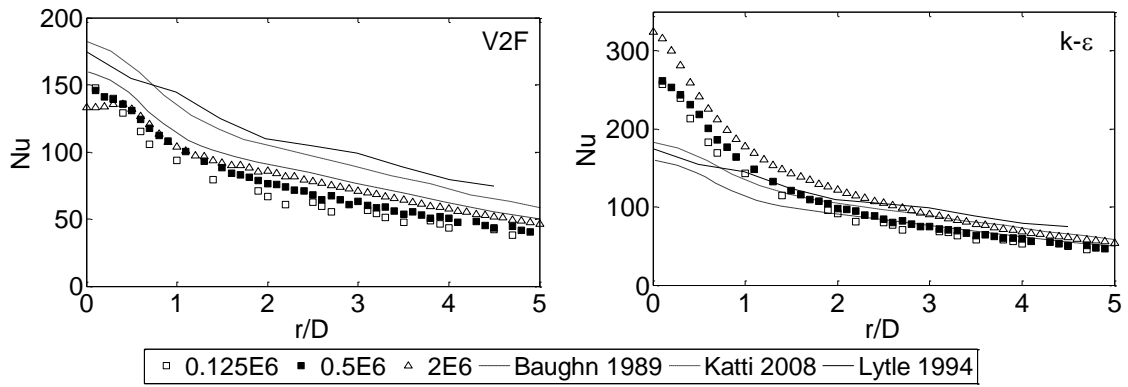


Figure 17. Effect of mesh density in wall-parallel direction the Nu (URANS models).

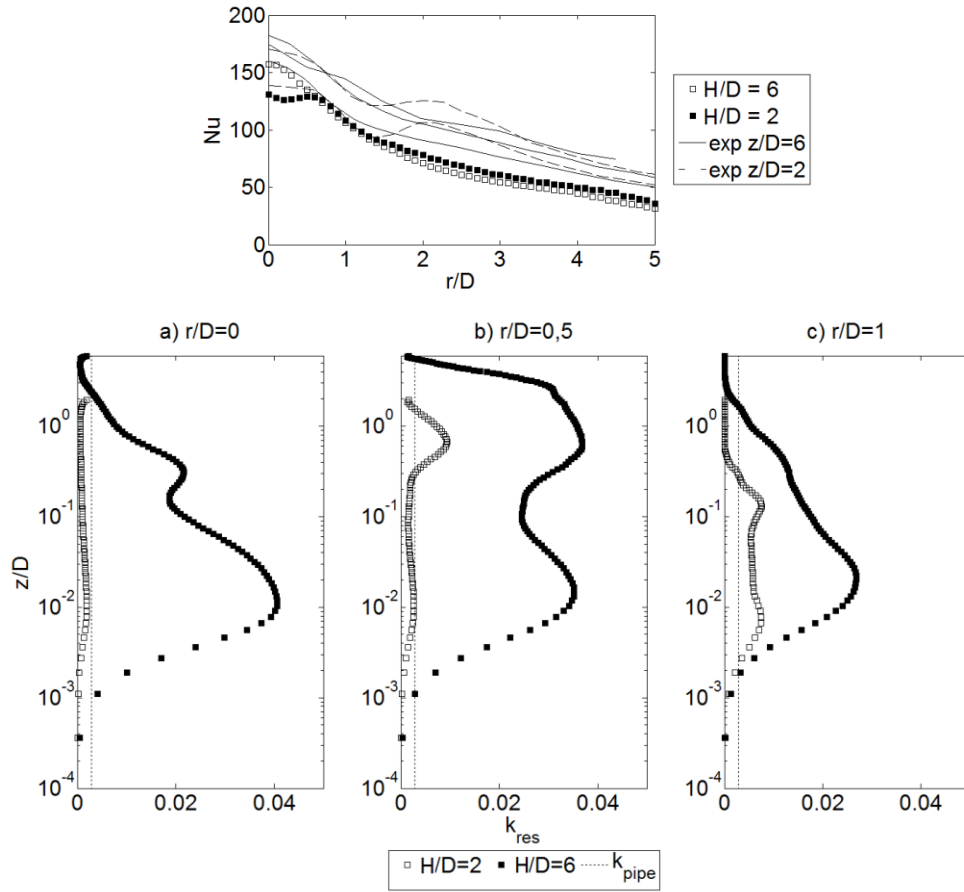


Figure 18. (top) Nu prediction for H/D=2 and H/D=6 using LES model. (bottom) k_{res} for H/D=2 and H/D=6 using LES model. For reference fully developed pipe flow “ k_{pipe} ”.

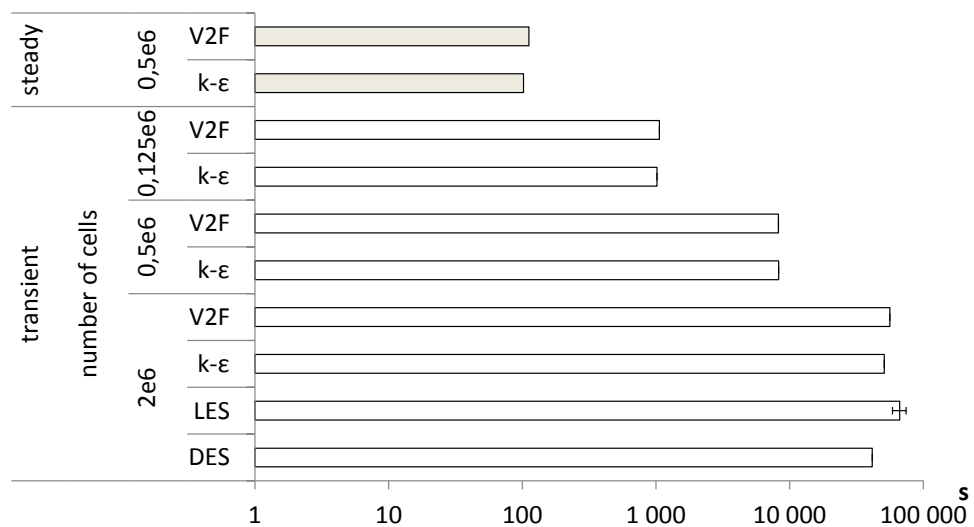


Figure 19. CPU real time per simulated second. More than one simulation is run with the LES model, the error bar corresponds to one standard deviation.